The following publication S. Li, K. T. Chau, W. Liu, J. Guo, C. Liu and Y. Hou, "A Wireless Permanent-Magnet Brushless DC Motor Using Contactless Feedback and Autonomous Commutation," in IEEE Transactions on Power Electronics, vol. 40, no. 7, pp. 10140-10153, July 2025 is available at https://doi.org/10.1109/TPEL.2025.3543572.

# A Wireless Permanent-Magnet Brushless DC Motor Using Contactless Feedback and Autonomous Commutation

Songtao Li, Graduate Student Member, IEEE, K.T. Chau, Fellow, IEEE, Wei Liu, Senior Member, IEEE, Jian Guo, Member, IEEE, Chunhua Liu, Senior Member, IEEE, and Yunhe Hou, Senior Member, IEEE

Abstract—This article proposes and implements a wireless permanent-magnet brushless DC (PM-BLDC) motor, which realizes precise closed-loop speed control and autonomous commutation by offering rotor position feedback in a contactless approach. To reduce the system complexity, a three-phase fourswitch (TPFS) inverter is newly used to control the wireless motor. Incorporated with two orthogonal bipolar coils, the highorder compensation network provides four decoupled current paths to control the four self-drive switches in the TPFS inverter. By changing the frequency of the wireless power transfer, the motor phases can be properly energized to ensure a smooth operation in both directions without any microcontrollers at the secondary side. To equalize the motor current transmitted under different frequencies across a wide speed range, sigma-delta modulated pulse frequency modulation ( $\Sigma$ - $\Delta$  PFM) is adopted together with pulse width modulation (PWM), which also achieves higher efficiency and fewer effects from unexpected harmonics. The feasibility of the proposed design is validated by prototyping and testing a 4000-rpm 134-W PM-BLDC motor platform. Experimentations verify that the proposed wireless PM-BLDC motor achieves reliable commutation and precise speed tracking against load variations using contactless feedback.

Index Terms—Wireless power transfer, wireless permanent-magnet brushless DC motor, contactless feedback, autonomous commutation, pulse frequency modulation.

### I. INTRODUCTION

W IRELESS power transfer (WPT) has attracted much attention from industries and academic researchers in recent years [1]. The non-contact power transmission eliminates both physical and electrical connections between the power source and the energized equipment [2], bringing unique benefits of convenience, flexibility, electrical spark protection, enhanced stability, and longer lifespan in watery

This work was supported in part by the Hong Kong Research Grants Council, Hong Kong Special Administrative Region, China, under Grant T23-701/20-R, and in part by The Hong Kong Polytechnic University under Grant P0048560. (Corresponding author: K.T. Chau.)

Songtao Li, Jian Guo, and Yunhe Hou are with the Department of Electrical and Electronic Engineering, The University of Hong Kong, Hong Kong, China (e-mail: stli@eee.hku.hk; guojian@eee.hku.hk; yhhou@eee.hku.hk).

K.T. Chau and Wei Liu are with the Research Centre for Electric Vehicles and Department of Electrical and Electronic Engineering, The Hong Kong Polytechnic University, Hong Kong, China (e-mail: k.t.chau@polyu.edu.hk; wei.liu@polyu.edu.hk).

Chunhua Liu is with the School of Energy and Environment, City University of Hong Kong, Hong Kong, China (e-mail: chunliu@cityu.edu.hk).

and harsh environments [3], [4]. The WPT has been commercialized in the charging systems of hand-held equipment [5], and also expanding its applications into the charging of electric vehicles [6], [7], and unmanned aerial vehicles [8]. Apart from wireless charging, the electrical energy transmitted through WPT can be converted to other forms such as wireless lighting, wireless heating, and wireless motoring [9].

Wireless motoring converts electrical energy to mechanical energy directly without any physical contact, which allows the wireless motors to work in a sealed environment for better adaptability against environmental impacts [10]. Furthermore, it provides the possibility to remove the energy storage module of automated guided vehicles and mobile robots for a more compact size and also extend the continuous working time limited by the energy storage volume.

Based on the structure of the control scheme, the wireless motors can be classified into dual-controller wireless motors and primary-controlled wireless motors. In the dual-controller scheme, the motor is powered by WPT, while all the motor control is applied by an extra motor controller at the secondary side [11]. Due to the wired connection between the motor controller and the secondary side circuit, traditional motor control methods can be easily incorporated into the system. Similar structures have been introduced in several designs of wireless permanent-magnet synchronous motors [12]-[14]. However, for sealed working environments, the fragile motor controller brings a huge need for maintenance. To solve this problem, different types of primary-controlled wireless motors have emerged, where both the WPT and motor control are realized in a single controller at the primary side. Usually, multiple power channels are generated by using multiple pairs of magnetic coils [15], [16] or multi-frequency resonant networks [17], [18], by changing the transmitting frequency, currents are fed into different motor windings with expected directions.

The precise control of wireless motors plays a crucial role in unleashing the full performance of the motor and ensuring stable operation. However, acquiring the feedback of wireless motors is challenging because of the contactless structure. For most of the existing primary-controlled wireless motors, feedback control is not included [15], [17], [19], and it is hard to adjust the motor speed to a specific value and maintain the speed with variable loads. The wireless stepper motor offers speed and position control capabilities without using any sensors at the secondary side [18], however, the motor is not suitable for high-speed applications. Several attempts have

© 2025 IEEE. Personal use of this material is permitted. Permission from IEEE must be obtained for all other uses, in any current or future media, including reprinting/republishing this material for advertising or promotional purposes, creating new collective works, for resale or redistribution to servers or lists, or reuse of any copyrighted component of this work in other works.

been made to provide contactless feedback. The wireless switched reluctance motor (SRM) designed in [20] and [21] use a Bluetooth module and a wireless resolver for commutation control, respectively. The Bluetooth module transmits the exact rotor positions measured by a position sensor, but the latency of communication cannot be ignored at high speeds, causing commutation failure. The wireless resolver has better real-time performance, however, it suffers from low resolution and bulky size. The photoelectric encoder adopted in [22] provides position feedback for speed and position control. The rotating grid attached to the motor shaft can be easily damaged and the accuracy might be affected by humidity change.

In the operating process, the amplitude of the motor current is adjusted to reach and maintain the desired speed with various load conditions. For a multi-frequency wireless motor system, the motor current is generated by the WPT output in different transmitting frequencies [17]. Therefore, the system should provide a wide output range while keeping the balance of output under different transmitting frequencies. Among the existing methods for output regulation, pulse width modulation (PWM) is widely accepted due to its simplicity [18]. To reduce the switching loss in a wide output range, pulse frequency modulation (PFM) and pulse density modulation are also adopted in WPT systems [11]. The harmonics induced by different modulation methods affect the system's operation, by choosing the proper modulation methods and transmitting frequencies, the system can achieve higher efficiency.

The permanent-magnet brushless DC (PM-BLDC) motor has been widely applied in electric vehicles, water pumping, household appliances, and industrial manufacturing, due to its advantages of high efficiency, high power density, and long lifespan [23]. However, compared with a brushed DC motor [15], the rotor position is essential for commutation, usually, a Hall effect sensor is integrated to provide rotor position. Although sensorless control has been incorporated into the wired control scheme [23], the direct measurement of back electromotive force (EMF) needed for position estimation [24] is challenging in the wireless scheme. Thus, providing position feedback in the contactless approach is more reliable in wireless motor systems.

In this paper, a wireless PM-BLDC motor is newly proposed and implemented, which offers autonomous commutation and precise speed control. A wireless-powered Hall effect sensor modulates the load in the feedback channel according to its output, thus, the rotor position is related to a specific current amplitude at the transmitter side, providing contactless position feedback. To reduce the system's size and cost, a three-phase four-switch (TPFS) inverter is adopted, and each switch can be controlled independently by the self-drive circuit connected to a decoupled current path. To achieve higher efficiency while reducing misconduct caused by harmonics generated in the output tuning process, the proposed system adopts a hybrid modulation including PWM and sigma-delta modulated PFM ( $\Sigma$ - $\Delta$  PFM) [25]. Compared with the existing wireless PM-BLDC motor [26] where feedback control is not discussed, the proposed system realizes both power and control in the fully wireless approach.

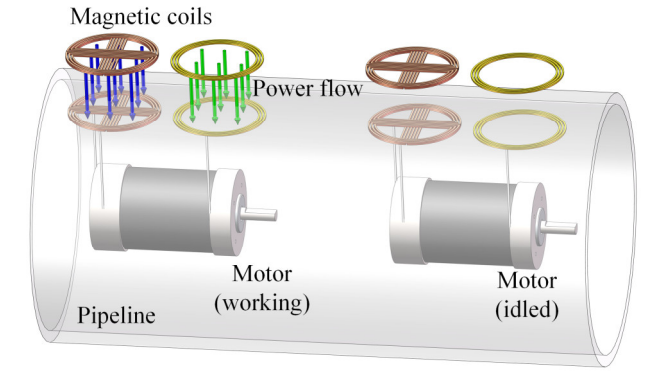


Fig. 1. Application of proposed wireless PM-BLDC motor in underground pipeline networks.

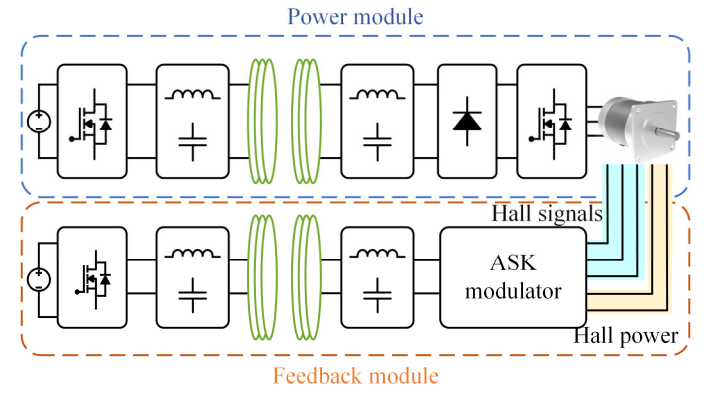


Fig. 2. System configuration of proposed wireless PM-BLDC motor.

The electrical and physical isolation of the proposed system brings huge advantages in the application of underground pipeline networks [19], driving the motors sealed in the pipe without breaking the integrity of the pipe, as shown in Fig. 1. Also, it has potential applications in mobile robots [27] and industrial manufacturing facilities [18].

The rest of the article is organized as follows: Section II will introduce the system configuration and commutation strategy using a self-drive TPFS inverter. Section III will present the characteristics of the compensation network in power and feedback modules and also present the design of magnetic coils with simulation results. Section IV will discuss the contactless feedback control, the hybrid modulation, and the frequency selection. In Section V, an experimental prototype will be constructed and tested to verify the feasibility of the proposed wireless PM-BLDC motor. Finally, Section VI will conclude this article.

# II. SYSTEM CONFIGURATION AND CONTROL PRINCIPLE

# A. System Configuration

The system configuration of the proposed wireless PM-BLDC motor is shown in Fig. 2, where the whole system is split into a power module and a feedback module. The power module connects to the motor phases directly, feeding power to the windings wirelessly in a proper sequence according to the direction and feedback. To drive the motor with a reduced number of switches, a three-phase four-switch (TPFS) inverter is adopted at the secondary side, and all the switches are equipped with self-drive circuits connected to the

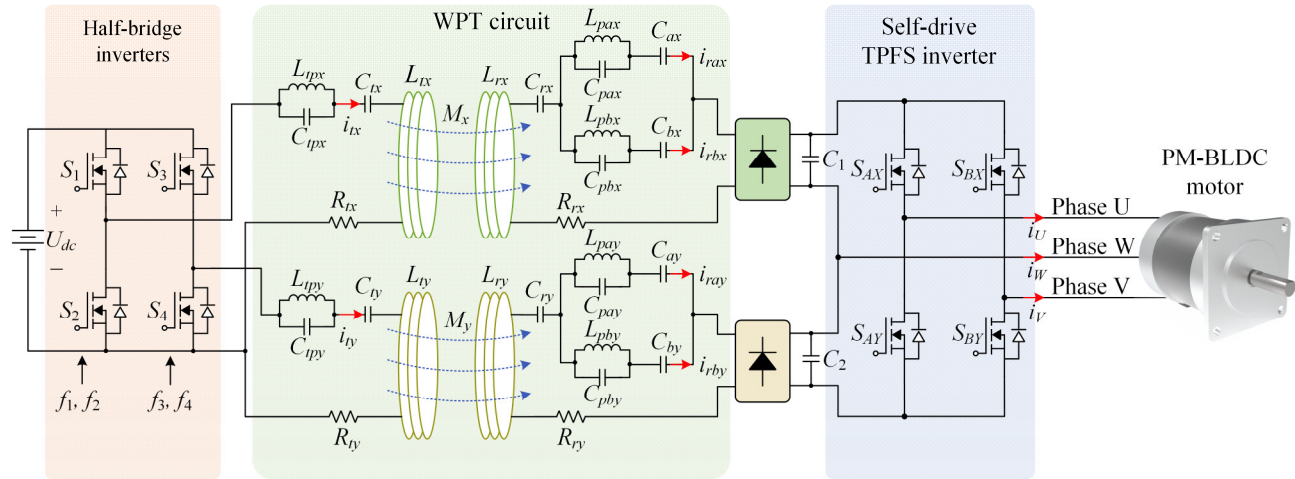


Fig. 3. Circuit topology of power module.

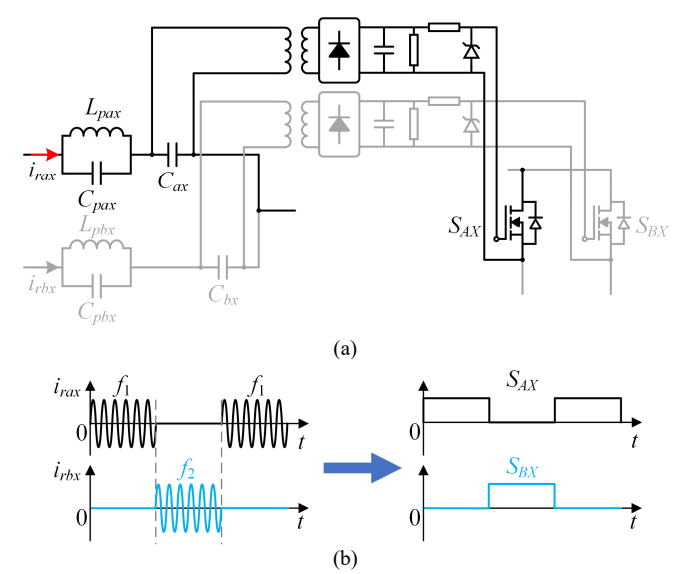


Fig. 4. Circuit topology and control signals generation of self-drive switches in channel X. (a) Self-drive circuit topology. (b) Theoretical waveform of switch control signals in channel X.

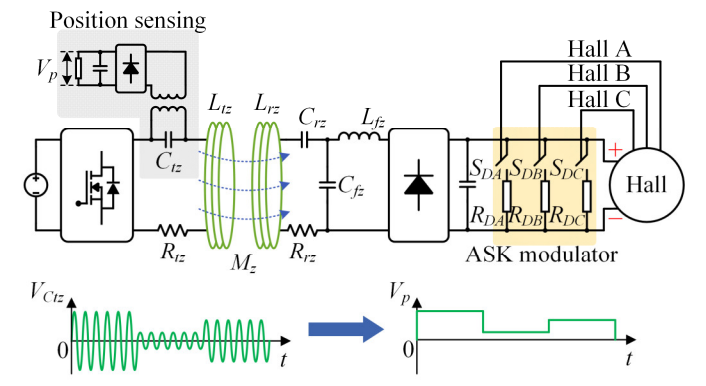


Fig. 5. Circuit topology and configuration of feedback module.

compensation network. For wireless power transmission, decoupled magnetic coils and high-order compensation circuits are involved to provide multiple resonant frequencies and four decoupled current paths. By changing the transmitting frequency, all the switches in the TPFS inverter can be controlled individually. Totally, four transmitting frequencies  $(f_1, f_2, f_3, \text{ and } f_4)$  are used. The feedback module is

a WPT channel isolated from the power module, feeding power to the Hall effect sensor attached to the motor. To help read the sensor measurements from the primary side, a load modulator using amplitude-shift keying (ASK) is connected in parallel to the Hall effect sensor. The equivalent load of the feedback channel is modulated according to the sensor output, leading to a change in the current amplitude of the transmitter circuit. Therefore, the amplitude levels represent the Hall states related to rotor positions.

Fig. 3 shows the circuit topology of the power module.  $L_{tx}$ ,  $L_{rx}$ ,  $L_{ty}$ ,  $L_{ry}$ ,  $R_{tx}$ ,  $R_{rx}$ ,  $R_{ty}$ , and  $R_{ry}$  with subscripts x and y denote the magnetic coils and their internal resistances in channels X and Y. The compensation circuit has the same topology in both channels. Take channel X as an example,  $L_{tpx}$ ,  $C_{tpx}$ , and  $C_{tx}$ constitute the compensation network at the primary side, while  $C_{rx}$ ,  $L_{pax}$ ,  $C_{pax}$ ,  $C_{ax}$ ,  $L_{pbx}$ ,  $C_{pbx}$ , and  $C_{bx}$  constitute the compensation network at the secondary side, wherein, two parallel-connected LC tanks ( $L_{pax}$ ,  $C_{pax}$ ,  $L_{pbx}$ , and  $C_{pbx}$ ) are tuned as band-stop filters to provide separate current paths for each transmitting frequency. The self-drive switches of the TPFS inverter ( $S_{AX}$ ,  $S_{BX}$ ,  $S_{AY}$ , and  $S_{BY}$ ) extract control signals from  $C_{ax}$ ,  $C_{bx}$ ,  $C_{ay}$ , and  $C_{by}$ . Phase U and V of the PM-BLDC motor are connected to the two branches of the TPFS inverter, while phase W is connected to the middle point of the DC-link capacitors ( $C_1$  and  $C_2$ ).  $i_{tx}$ ,  $i_{ty}$ ,  $i_{rax}$ ,  $i_{rbx}$ ,  $i_{ray}$ , and  $i_{rby}$  represent the currents in the two transmitters and the four current paths for signal extraction.  $i_U$ ,  $i_W$ ,  $i_V$  denote the currents injected into the motor windings U, W, and V, respectively. Fig. 4 shows the circuit topology and operating principle of the self-drive switches in channel X, when channel X operates in  $f_1$ ,  $S_{AX}$  turns on, while  $S_{BX}$  only turns on when operating under  $f_2$ . The

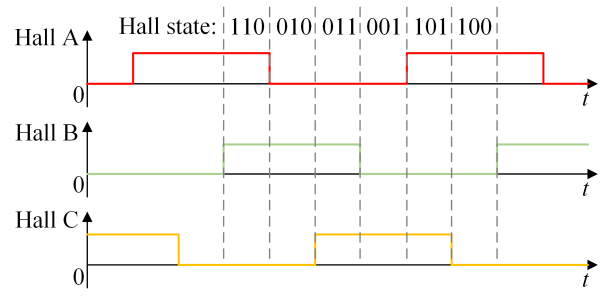


Fig. 6. Theoretical Hall sensor outputs.

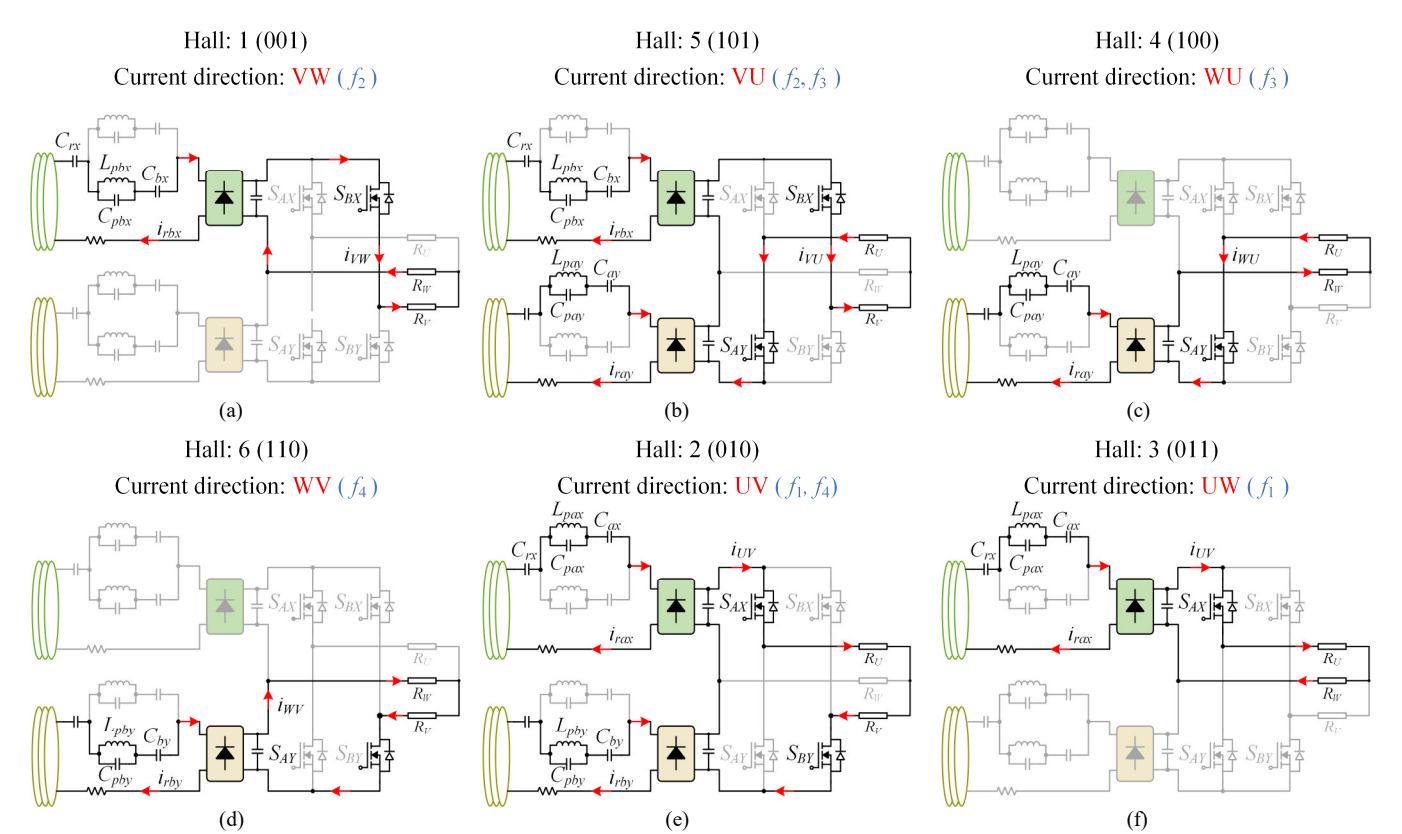


Fig. 7 Commutation strategy and corresponding WPT current paths when rotating in CCW direction. (a) Sensor output is 1. (b) Sensor output is 5. (c) Sensor output is 4. (d) Sensor output is 6. (e) Sensor output is 2. (f) Sensor output is 3.

circuit topology and configuration of the feedback module are shown in Fig. 5.  $L_{tz}$  is the transmitter coil, compensated by a series-connected capacitor  $C_{tz}$ ;  $L_{rz}$  is the receiver coil, compensated by inductor-capacitor-capacitor (LCC) network  $(L_{fz}, C_{rz}, C_{fz})$ .  $R_{tz}$  and  $R_{rz}$  represent the internal resistances of the coils in the feedback module. The motor-attached Hall effect sensor is powered as the load together with an ASK modulator. The modulator contains three resistors  $R_{DA}$ ,  $R_{DB}$ , and  $R_{DC}$ , each connects to a MOSFET ( $S_{DA}$ ,  $S_{DB}$ , and  $S_{DC}$ ). The outputs of the Hall effect sensor are converted to drive the MOSFETs through the isolated switch driver, therefore, the equivalent load of the feedback module is modulated according to the sensor output. As shown in Fig. 6, the three Hall sensor outputs are composed of six Hall states in the rotation. Thus, six different equivalent load values are generated. The current amplitude in the primary side is measured to reflect the rotor position. To reduce the hardware cost and avoid excessively high sample rate, the highfrequency voltage over  $C_{tz}$  is isolated by a transformer, rectified, and then stabilized to a DC value  $V_p$ .  $V_p$  is then sampled by the controller to provide position feedback for commutation and speed control.

# B. Commutation Strategy

The commutation of a PM-BLDC motor is conducted according to the angular position of the rotor. By applying current to the stator windings with different directions, their magnetic poles are changed to cause continuous movement of the rotor with steady torque output. For a conventional wired three-phase PM-BLDC motor, the six-step commutation is generally adopted, including 120-degree conduction mode and

180-degree conduction mode [24]. In the proposed wireless PM-BLDC motor, the 120-degree conduction mode is realized through the self-drive TPFS inverter. To drive the motor in the counterclockwise (CCW) direction, the stator windings are energized in a different looped sequence of VW  $\rightarrow$  VU  $\rightarrow$  $WU \rightarrow WV \rightarrow UV \rightarrow UW$ , with corresponding transmitting frequencies  $f_2 \rightarrow f_2 f_3 \rightarrow f_3 \rightarrow f_4 \rightarrow f_1 f_4 \rightarrow f_1$ . Fig. 7 shows the six commutation steps and their corresponding current paths when rotating CCW, wherein, the motor is simplified as Yconnected resistive loads (Ru, Rv, Rw) to better describe the current direction. Take two steps as examples, when the Hall state is 5, power is transmitted from the primary side in both channels in  $f_2$  and  $f_3$ , respectively, thus,  $S_{AY}$  and  $S_{BX}$  are switched on while the other switches are turned off. The current is injected into phase V and flows out from phase U. When the Hall state is changed to 4, channel X is idled while channel Y remains transferring in  $f_3$ . Only  $S_{AY}$  is switched on and the current flows from  $R_W$  to  $R_U$ . Following the same principle, all the currents required for the six-step commutation can be realized with the proposed system. To operate with the clockwise (CW) direction, the stator windings are energized in a different looped sequence of VW  $\rightarrow$  UW  $\rightarrow$ UV → WV → WU → VU, with the corresponding transmitting frequencies  $f_2 \rightarrow f_1 \rightarrow f_1 f_4 \rightarrow f_4 \rightarrow f_3 \rightarrow f_2 f_3$ .

### III. DESIGN OF COMPENSATION NETWORK

The characteristic of the compensation network plays a decisive role in the performance of the WPT system. By choosing appropriate compensation topologies, the system can realize load-independent constant current (CC) output or

constant voltage (CV) output at specified resonant frequencies [28]. Since the motor can be regarded as an adjustable load that varies with operating conditions, the WPT system with load-independent CC output is more suitable for driving the motor while keeping a stable control signal for self-drive switches. In the power module of the proposed design, four resonant frequencies ( $f_1=150$  kHz,  $f_2=300$  kHz,  $f_3=125$  kHz, and f<sub>4</sub>=250 kHz) are adopted to control the four self-drive switches independently. Separated by two pairs of decoupled magnetic coils, each power channel is designed to have two resonant frequencies, and the parameters of inductors and capacitors are tuned to provide load-independent CC output at each resonant frequency with different loads. However, in the feedback module, the output voltage should be limited to ensure the safe operation of the Hall effect sensor and also the ASK modulator. Therefore, the compensation network is designed to offer load-independent CV output. The operating frequency is set as  $f_5$ =400 kHz to reduce the possible interference from the power channel.

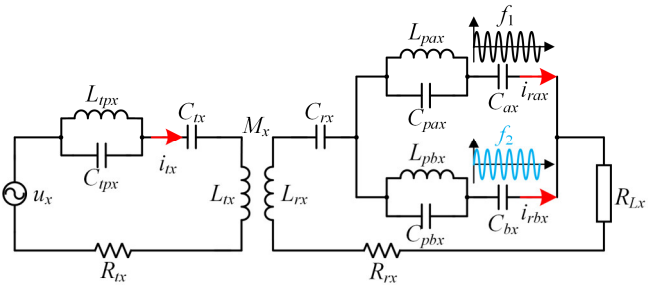
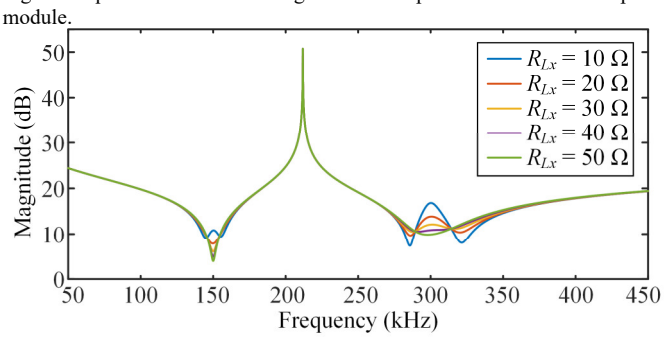


Fig. 8. Equivalent circuit of high-order compensation network in power



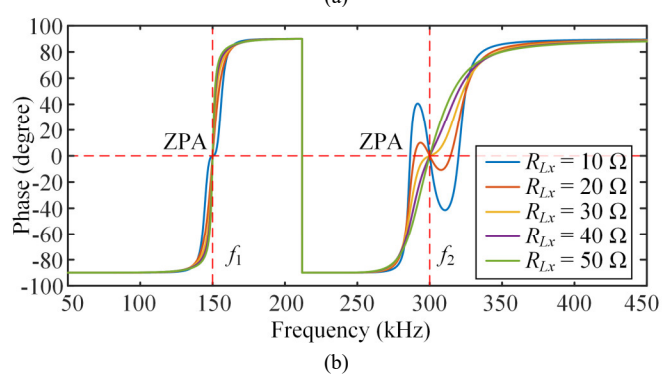


Fig. 9. Impedance characteristic of compensation network in power module. (a) Impedance magnitude against various loads. (b) Impedance angle against various loads.

# A. High-order Compensation Network in Power Module

The compensation network in the power module is designed based on the previous work in [18]. Since the two power

channels have the same structure, only channel X is analyzed for exemplification. The equivalent circuit is shown in Fig. 8; to simplify the analysis, the self-drive switches and the motor are replaced by a resistive load  $R_{Lx}$ . Both the primary-side circuit and secondary-side circuit are designed to resonant at  $f_1$  and  $f_2$ , the current under different frequencies share the same route at the primary side and split into separate routes at the secondary side. The self-impedance of the primary-side circuit and secondary-side circuit is given by

$$Z_{tx} = R_{tx} + j\omega L_{tx} + \frac{1}{j\omega C_{tx}} + \frac{j\omega L_{tpx}}{1 - \omega^2 L_{tpx} C_{tpx}}$$
(1)

$$Z_{rx} = R_{rx} + R_{Lx} + j\omega L_{rx} + \frac{1}{j\omega C_{rx}} + \frac{Z_{ax}Z_{bx}}{Z_{ax} + Z_{bx}}$$
(2)

where  $Z_{ax}$  and  $Z_{bx}$  are the impedance of the decoupled branches, shown as

$$Z_{ax} = \frac{1}{j\omega C_{ax}} + \frac{j\omega L_{pax}}{1 - \omega^2 L_{pax} C_{pax}}$$
(3)

$$Z_{bx} = \frac{1}{j\omega C_{bx}} + \frac{j\omega L_{pbx}}{1 - \omega^2 L_{pbx} C_{pbx}} \tag{4}$$

When working under resonant frequencies, self-impedances on both sides are greatly reduced by eliminating the imaginary part, which are expressed as

$$\operatorname{Im}(Z_{tx}) = 0$$
,  $\operatorname{Im}(Z_{tx}) = 0$  (5)

The primary-side compensation network is composed of a series-connected LC ( $L_{tx}$ ,  $C_{tx}$ ) and parallel-connected LC ( $L_{tpx}$ ,  $C_{tpx}$ ), providing two resonant frequencies. Based on (1) and (5), with predefined  $f_1$ ,  $f_2$ ,  $L_{tx}$ , and  $L_{tpx}$ , the capacitances  $C_{tx}$  and  $C_{tpx}$  can be calculated as

$$\begin{cases} C_{tx} = \frac{\omega_1^2 + \omega_2^2 \pm \sqrt{\Delta}}{2(L_{tpx} + L_{tx})\omega_1^2 \omega_2^2} \\ C_{tpx} = \frac{(\omega_1^2 + \omega_2^2) \mp \sqrt{\Delta}}{2\omega_1^2 \omega_2^2 L_{tpx}} \end{cases}$$
(6)

where

$$\Delta = (\omega_1^2 - \omega_2^2)^2 - \frac{4L_{tpx}\omega_1^2\omega_2^2}{L_{tr}}$$
 (7)

To ensure a real solution,  $\Delta$  should be positive. By defining the ratio of resonant frequencies and inductances, the constraints in (7) can be further expressed as

$$r_L > \frac{4r_f^2}{\left(r_f^2 - 1\right)^2}$$
 (8)

wherein,  $r_L = L_{tx}/L_{tpx}$ ,  $r_f = f_2/f_1$ .

The compensation network at the secondary side provides two decoupled current paths using one receiver coil. The two parallel-connected LC tanks are designed as band-stop filters to provide maximum impedance at the frequency resonant at the other branch, thus, the parameters should satisfy

$$\begin{cases} \omega_{l} = \frac{1}{2\pi\sqrt{L_{pbx}C_{pbx}}} \\ \omega_{2} = \frac{1}{2\pi\sqrt{L_{pax}C_{pax}}} \end{cases}$$
(9)

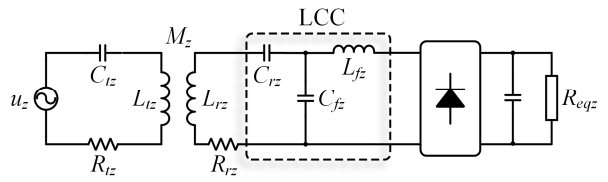


Fig. 10. Equivalent circuit of compensation network in feedback module.

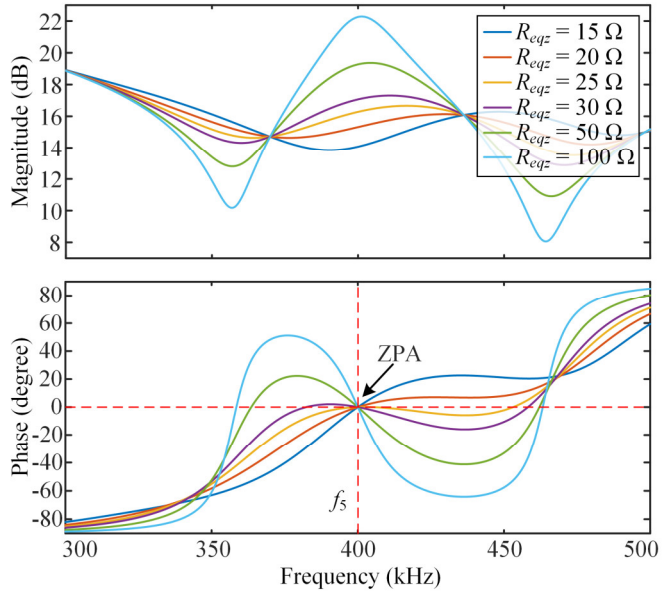


Fig. 11. Input impedance characteristics of compensation network in feedback module.

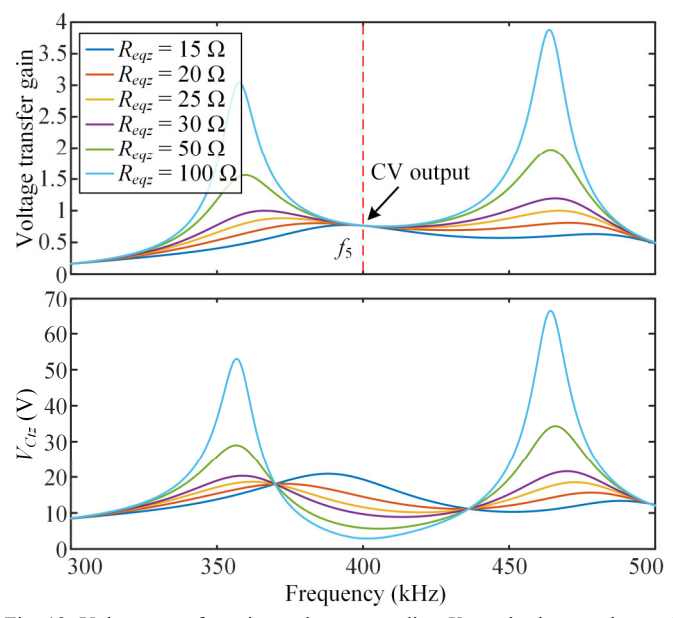


Fig. 12. Voltage transfer gains and corresponding  $V_{\rm ctz}$  under input voltage of 10 V.

Therefore,  $i_{rax}$  flowing through  $C_{ax}$  only includes the component with frequency  $f_1$ , and  $i_{rbx}$  is under frequency  $f_2$ . Then,  $U_{Cax}$  and  $U_{Cbx}$  are extracted to control the switches. The amplitude of the switch control signals is mainly affected by the amplitude of  $i_{rax}$ ,  $i_{rbx}$ , and also the capacitances of  $C_{pax}$ ,  $C_{pbx}$ . In the proposed system, the switch control signals are designed to reach the value at which the MOSFETs have the lowest on-state resistance with rated motor current, as given by

$$\begin{cases}
C_{ax} = \frac{I_{rated}}{j\omega_{1}\alpha U_{S}} \\
C_{bx} = \frac{I_{rated}}{j\omega_{2}\alpha U_{S}}
\end{cases}$$
(10)

where  $I_{rated}$  is the rated current of the motor,  $U_S$  is the optimal gate-source voltage of MOSFET, and  $\alpha$  represents the turns ratio of the isolated transformer in self-drive circuits. According to (2), (5), and (9), the secondary-side circuit achieves full resonance at  $f_1$  and  $f_2$ , which are given by

$$\begin{cases} j\omega_{1}L_{rx} + \frac{1}{j\omega_{1}C_{rx}} + \frac{j\omega_{1}L_{pax}}{1 - \omega_{1}^{2}L_{pax}C_{pax}} + \frac{1}{j\omega_{1}C_{ax}} = 0\\ j\omega_{2}L_{rx} + \frac{1}{j\omega_{2}C_{rx}} + \frac{j\omega_{2}L_{pbx}}{1 - \omega_{2}^{2}L_{pbx}C_{pbx}} + \frac{1}{j\omega_{2}C_{bx}} = 0 \end{cases}$$
(11)

Fig. 9 shows the magnitude and phase of the input impedance of the whole system. With a variable load, the phase angle remains zero at  $f_1$  and  $f_2$ , thus achieving robust zero-phase-angle (ZPA) operation.

# B. Compensation Network in Feedback Module

The feedback module provides load-independent CV output to ensure the safe operation of the Hall effect sensor and the modulator. Previous research has revealed that some compensation topologies can achieve such characteristics under a certain frequency. The series-series (S-S) compensation can achieve CV output with the simplest structure [29], however, the operating frequencies with CV output are different from the resonant frequency, resulting in larger power consumption. The double-sided LCC circuit can achieve ZPA operation with CV output, while the high-order compensation circuit increases the volume and complexity [28]. In the proposed design, an S-LCC compensation topology is adopted to reach a balance between ZPA operation and the system complexity, the equivalent circuit of the feedback module is shown in Fig. 10. The whole circuit is designed to resonant at  $f_5$ , satisfying the following relationship:

$$\omega_5^2 L_{rz} C_{rz} = 1 \tag{12}$$

$$j\left(\omega_{5}L_{rz} - \frac{1}{\omega_{5}C_{rz}}\right) = j\omega_{5}L_{fz} = \frac{j}{\omega_{5}C_{fz}}$$
(13)

Therefore, the total input impedance of the source  $u_z$  can be expressed as

$$Z_{inz} = j \left( \omega L_{tz} - \frac{1}{\omega C_{tz}} \right) + R_{tz} + \frac{\omega^2 M_z^2}{Z_{rotz}}$$
 (14)

where

$$Z_{refz} = j \left( \omega L_{rz} - \frac{1}{\omega C_{rz}} \right) + R_{rz} + \frac{1}{j \omega C_{fz}} \| \left( j \omega L_{fz} + \frac{8}{\pi^2} R_{eqz} \right) (15)$$

As depicted in Fig. 11, the compensation network in the feedback module achieves ZPA operation at frequency  $f_5$ , and the input impedance varies with the load. As the primary side is compensated by a single capacitor  $C_{tz}$ , the voltage over  $V_p$  reflects the impedance variation. In Fig. 12, when the system operates under  $f_5$ , the voltage gain remains constant, while  $V_{Ctz}$  is changed by the load. Therefore, by modulating the load resistance  $R_{eqz}$  according to the sensor output, each Hall state

of the PM-BLDC motor will have a unique  $V_{Clz}$  value, providing the position feedback for the commutation and speed control. With no need to transmit the signal backward, both the circuit and the control are greatly simplified.

# C. Design of WPT Coils

The proposed wireless PM-BLDC motor has four independent current channels for self-drive switch control. Following the previous design in [18], two orthogonal bipolar coils are adopted to reduce the occupied space and eliminate the interference between the unrelated coils. In the feedback module, circular magnetic coils are adopted for better coupling, placed beside the power coils with a distance of 450 mm between each center. Fig. 13 shows the geometric dimensions of the magnetic coils in both modules and their relative position. A finite element analysis (FEA) model is built according to the geometric parameters shown in Fig. 13. Fig. 14 presents the current densities and magnetic field distribution along the middle parallel plane between the transmitters and the receivers. When energizing one power channel only, nearly no current is induced in another power channel as well as the feedback module, which proves that the power channels are decoupled by the orthogonal bipolar coils, and the interference to the feedback module is eliminated.

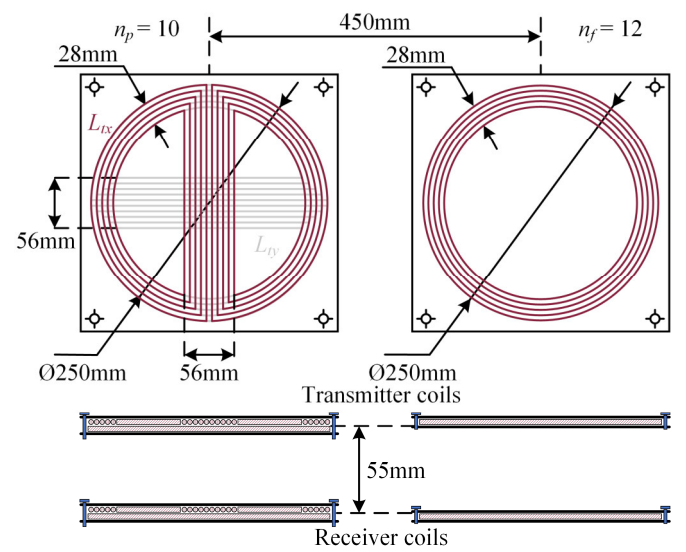
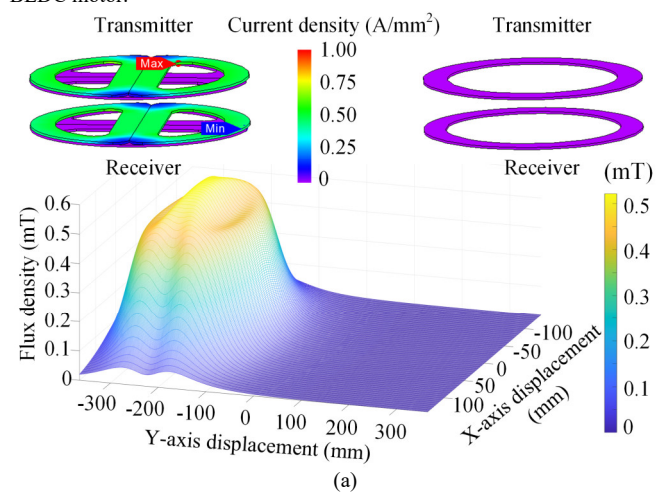


Fig. 13. Geometric dimension of magnetic coils in proposed wireless PM-BLDC motor.



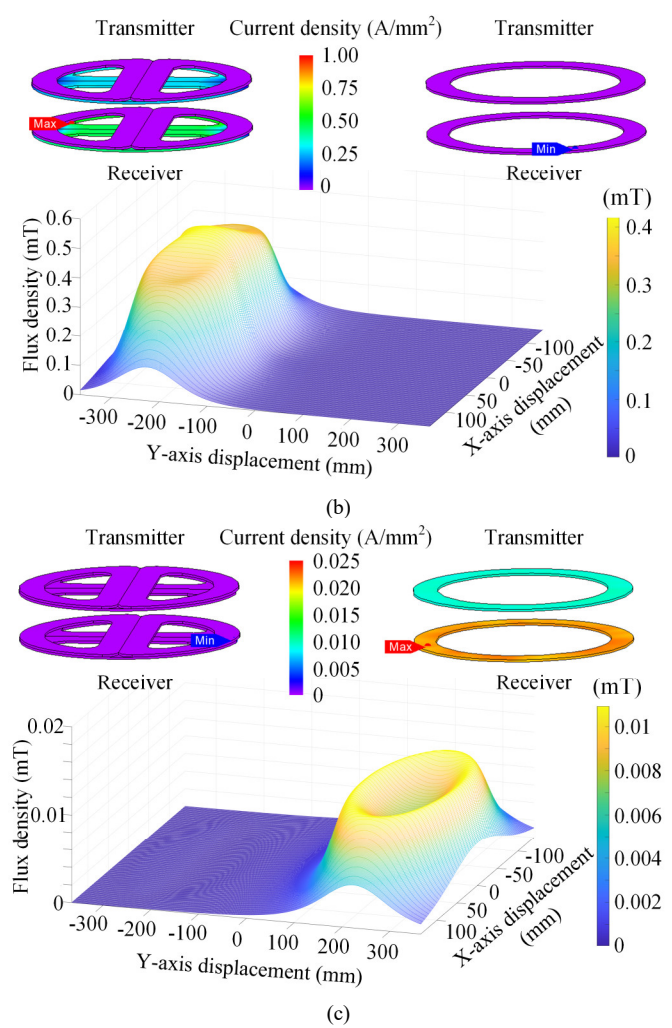


Fig. 14. FEA results of current densities and magnetic field distribution along middle parallel plane between magnetic coils. (a) Power module operating under frequency  $f_1$  with an output current of 5 A. (b) Power module operating under frequency  $f_4$  with an output current of 5 A. (c) Feedback module operating under frequency  $f_5$  with an output voltage of 5 V.

### IV. SYSTEM CONTROL

# A. Hybrid Modulation

For a closed-loop controlled wireless motor system, the motor currents need to be adjusted automatically to reach the reference speed under different loads. In previous research, DC-DC converters [30] and wireless energy modulation [11] are combined with WPT systems for various outputs. Compared with using extra converters, wireless energy modulation manipulates power directly with fewer electrical components, leading to a compact size and higher efficiency. Among the existing modulation strategies, PFM is developed for its wide-range soft switching and reduced average switching frequency, which makes it suitable for the proposed system. The PFM combines half cycles under different switching frequencies into a pulse sequence. Usually, the frequencies are selected as the WPT resonant frequency  $f_0$  and its subharmonics  $f_0/(2n_f+1)$ . A PFM duty ratio  $\delta_{PFM}$  is defined to describe the portion of the modulated amplitudes of the fundamental component to its maximum value, which can be expressed as [25]:

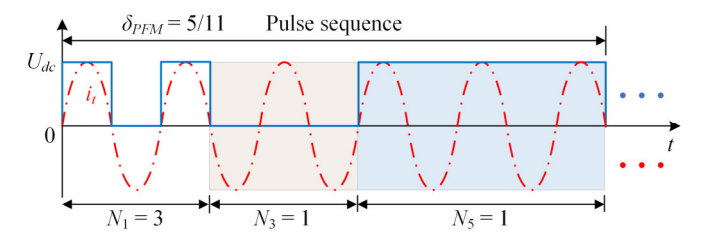


Fig. 15. Theoretical waveform of PFM output of a half-bridge inverter.

$$\delta_{PFM} = \frac{\sum_{n_f=0}^{n} N_{2n_f+1}}{\sum_{n_f=0}^{n} \left(2n_f+1\right) N_{2n_f+1}}$$
(16)

where  $N_{2f+1}$  denotes the number of half cycles under frequency  $f_0/(2n_f+1)$ . Furthermore, the period of the modulated pulse sequence is:

$$T_p = \sum_{n_f=0}^{n} N_{2n_f+1} T_{2n_f+1} / 2$$
 (17)

According to (16), the resolution and output range of the PFM are affected by the selected frequencies, to reach a smooth and precise regulation process,  $f_0$ ,  $f_0/3$ , and  $f_0/5$  are utilized in the proposed design. Fig. 15 is the theoretical waveform of the current and voltage output using PFM generated by a half-bridge inverter, when  $N_1$ =3,  $N_3$ =1, and  $N_5$ =1. As the pulse sequence involves multiple fundamental periods, the spectrum of voltage output contains subharmonics and interharmonics. The positions can be given by [31]:

$$f_h = \left(1 \pm \frac{j}{N_t}\right) f_0, j=1, 2, 3, ..., N_r - 1$$
 (18)

where  $N_{\rm i}=N_1+3N_3+5N_5$ . The number of harmonics is greatly increased in a longer pulse sequence, and the position varies within the process of output regulation. Compared with PWM, more harmonics are involved in the range below the fundamental frequency.

In the proposed system, two transmitting frequencies are utilized in each power channel. Because of the variation of the subharmonic and interharmonic positions in the whole regulation process, the harmonics close to the lower transmitting frequency will transmit power to the motor phase which should be idled. Therefore, to avoid misconduct, the PFM is only adopted when working under two lower frequencies  $f_1$  and  $f_3$ , while the higher frequencies  $f_2$  and  $f_4$  use PWM. As revealed in [32], no even-order harmonics are generated, to eliminate the interference from the harmonics, the WPT frequencies are set to satisfy  $f_2=2f_1$  and  $f_4=2f_3$ . Thus, the commutation can be completed by using the corresponding WPT frequency.

The PFM modulated signals are generated using a  $\Sigma$ - $\Delta$  modulator. As revealed in [25], the arrangement of the pulse sequence affects the harmonic amplitude and distribution with the same modulated pulse numbers. To suppress the output ripple and calculation burden, the PFM sequence is generated by a  $\Sigma$ - $\Delta$  modulator, which is depicted in Fig. 16. Fig. 17 shows the waveforms of the  $\Sigma$ - $\Delta$  PFM when  $\delta_{PFM}$ =17/27. With the help of  $\Sigma$ - $\Delta$  modulator, the half cycles with different frequencies are evenly distributed in the pulse sequence, leading to less output ripple.

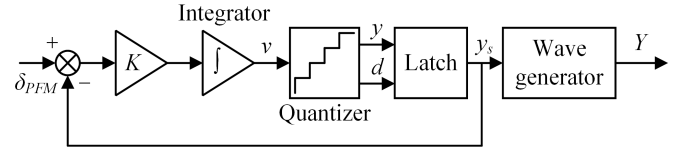


Fig. 16. Σ-Δ modulator for PFM generation of wireless PM-BLDC motor.

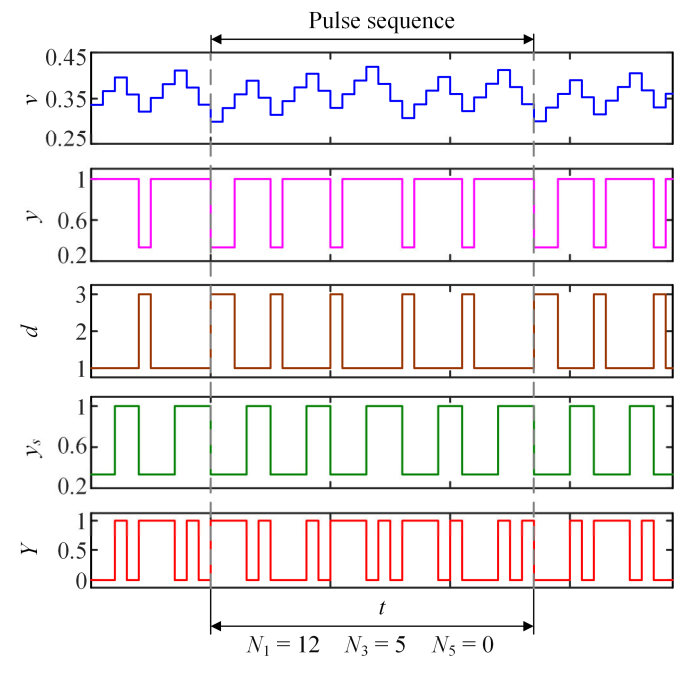


Fig. 17. Waveforms of  $\Sigma$ - $\Delta$  PFM when  $\delta_{PFM}$ =17/27 ( $N_1$ =12,  $N_3$ =5,  $N_5$ =0).

According to Fig. 7, the motor current in different commutation statuses is transmitted via wireless power under different frequencies. The motor currents should be equalized to ensure smooth operation within the whole speed and load range. In the proposed system, the output current under  $f_2$  is the lowest among the four frequencies and is selected as the reference. The output in other frequencies is tuned to reach the reference value, when neglecting the internal resistance of all the LC components, the duty ratios of the PFM and PWM can be derived based on the equivalent circuit in Fig. 8:

$$\begin{cases}
\delta_{PFM1} = \delta \frac{\omega_{1}}{\omega_{2}} \\
\delta_{PWM2} = \arcsin \delta / \pi
\end{cases}$$

$$\delta_{PFM3} = \delta \frac{\omega_{3} M_{y}}{\omega_{2} M_{x}}$$

$$\delta_{PWM4} = \arcsin \left( \delta \frac{\omega_{4} M_{y}}{\omega_{2} M_{x}} \right) / \pi$$
(19)

where,  $\delta$  is the output ratio of motor current,  $\delta_{PFM1}$ ,  $\delta_{PFM3}$ ,  $\delta_{PWM2}$ , and  $\delta_{PWM4}$  denote the PFM duty ratio in  $f_1$  and  $f_3$ , and the PWM duty ratio in  $f_2$  and  $f_4$ .

### B. Speed Control using Contactless Feedback

In the proposed wireless PM-BLDC motor, the rotor position modulated by the ASK modulator is sensed wirelessly at the primary side. However, for the traditional closed-loop speed control, motor currents are also sampled apart from position feedback. As the current sampling and the signal

transmission in wireless motors require auxiliary sampling circuits, real-time transmission modules, or microcontrollers, no current or voltage information is sampled in the proposed design. Therefore, to reduce the system complexity, a closed-loop speed control strategy is introduced based on contactless position feedback, as depicted in Fig. 18. The controller samples the voltage  $V_p$  and decides the WPT frequencies based on the corresponding Hall states, meanwhile, motor speed  $\omega_m$  is also calculated. Then, a PI controller is adopted to generate the output ratio  $\delta$  of the motor current. The duty ratios of PWM and PFM are calculated according to (19), respectively. Finally, the control signals for the primaryside inverter in the power module are generated using  $\Sigma$ - $\Delta$ modulator and PWM generator.

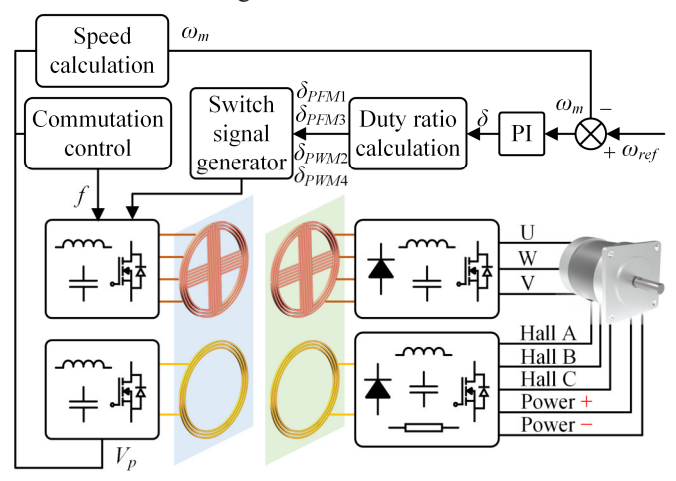


Fig. 18. Control diagram of proposed wireless PM-BLDC motor.

# V. EXPERIMENTAL VERIFICATION

# A. Prototype Experimentation and Verification

In order to verify the feasibility of the proposed wireless PM-BLDC motor, an experimental prototype was built, as shown in Fig. 19. The detailed parameters and specifications of the prototype are listed in Table I. The inverters of power module and feedback module are all equipped with silicon carbide (SiC) MOSFETs, as well as the self-drive TPFS inverter, with the model of IMW65R015M2H. The power diodes of the rectifiers at the secondary side are populated with STPS20120D. A three-phase PM-BLDC motor QBL5704-94-04-032 is adopted, with a rated power of 134 W, rated speed of 4000 rpm, and rated current of 5.08 A. The motor is loaded with a magnetic brake CD-HSY-20 with a maximum output torque of 2 N·m, and the Hall effect sensor is already integrated into the motor for position feedback. To measure the motor speed for evaluation, an incremental encoder E6B2-CWZ6C (2000 pulse/round) is attached to the motor shaft. In the feedback module, the ASK modulator uses TK8S06K3L N-channel MOSFET for load modulation, driven by isolated switch drivers TPSI3050QDWZRQ1. The whole system is controlled by a field-programmable gate array (FPGA) controller (XC7Z020-2CLG400I) with an AN9238 analog-to-digital converter (ADC) module. The decoupled WPT coils in the power module are wounded by 300×0.10 mm Litz wire, while 250×0.10 mm Litz wire is adopted for the WPT coil in the feedback module. All the waveforms are recorded by an 8-channel oscilloscope (Tektronix MSO58), and the system's efficiency is evaluated by a power analyzer (YOKOGAWA WT5000).

TABLE I
DESIGN PARAMETERS AND SPECIFICATIONS OF THE PROTOTYP

DESIGN PARAMETERS AND SPECIFICATIONS OF THE PROTOTYPE							
Parameters	Value/type	Unit					
Power module							
Transmitter coil inductances ( $L_{tx}$ , $L_{ty}$ )	53.15, 52.35	μН					
Receiver coil inductances $(L_{rx}, L_{ry})$	52.56, 53.01	μΗ					
Mutual inductances $(M_x, M_y)$	10.53, 10.44	μH					
Coil internal resistances	0.08, 0.08, 0.08,	Ω					
$(R_{tx}, R_{ty}, R_{rx}, R_{ry})$	0.08						
Transmitter compensated inductances	26.65, 26.27	μΗ					
$(L_{tpx}, L_{tpy})$							
Transmitter compensated capacitances	10.57, 15.44, 21.20,	nF					
$(C_{tx}, C_{ty}, C_{tpx}, C_{tpy})$	31.02						
Series-connected capacitances ( $C_{rx}$ , $C_{ry}$ )	14.18, 20.47	nF					
Band-stop filter capacitances	11.21, 12.74, 15.97,	nF					
$(C_{pax}, C_{pbx}, C_{pay}, C_{pby})$	18.38						
Band-stop filter inductances	25.31, 88.20, 25.55,	μΗ					
$(L_{pax}, L_{pbx}, L_{pay}, L_{pby})$	88.91						
Drive signal generation capacitances	181.23, 93.94,	nF					
$(C_{ax}, C_{bx}, C_{ay}, C_{by})$	218.09, 116.40						
Resonant frequencies $(f_1, f_2, f_3, f_4)$	149.40, 298.80,	kHz					
	125.21, 248.34						
Feedback mod	ule						
Transmitter coil inductance $L_{tz}$	58.80	μН					
Receiver coil inductance $L_{rz}$	59.22	μΗ					
Mutual inductance $M_z$	15.08	μΗ					
Transmitter compensated capacitance $C_{tz}$	3.33	nF					
Receiver compensated capacitance $C_{rz}$	3.88	nF					
Receiver filter capacitance $C_{fz}$	13.65	nF					
Receiver filter inductance $L_{fz}$	11.57	μΗ					
Resonant frequency $f_5$	403.22	kHz					
Modulation resistances ( $R_{DA}$ , $R_{DB}$ , $R_{DC}$ )	100, 50, 25.5	Ω					
Others							
Power module transformer (ratio)	ILR2-11-3 (2:1)						
Feedback module transformer (ratio)	ILR3-11-3 (3:1)						
Motor rated current	5.08	A					
Motor rated speed	4000	rpm					
Motor rated power	134	W					

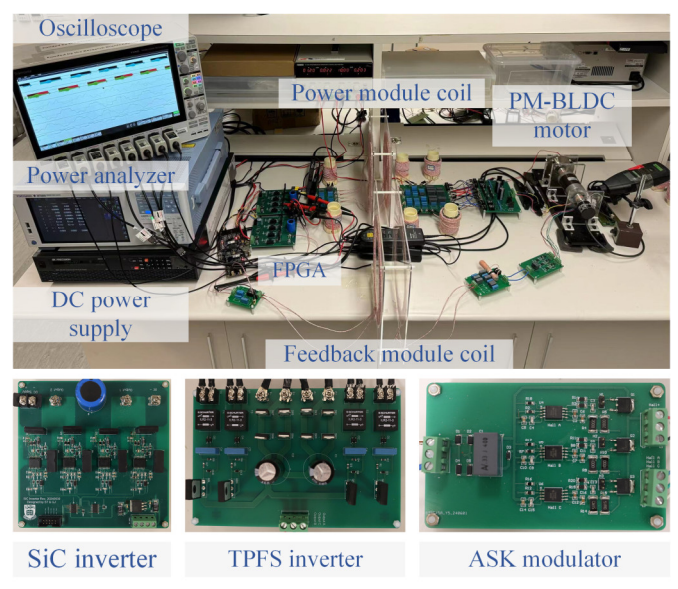


Fig. 19. Experimental setup of wireless PM-BLDC motor system.

First, the feasibility of the feedback module is tested. To simulate the motor operation, an AC servo motor Delta ECMA-C20602RS controlled by the servo drive Delta ASD-B2-0221-B is connected to the PM-BLDC motor, providing a constant speed of 500 rpm. Fig. 20 shows the waveform of inverter output voltage  $u_z$ , transmitter current  $i_{tz}$ , sensor output signals, and position signal  $V_p$  when rotating in the CCW direction and CW direction. The amplitude of  $i_{tz}$  has a unique value corresponding to each Hall state, thus generating different values of  $V_p$  for commutation and speed control. The values are only determined by the Hall state and are not affected by direction, which simplifies the process of determining the direction and calculating speed.

Second, the operation of the circuit as well as the performance of hybrid modulation is evaluated using a threephase Y-connected resistive load, with a 10  $\Omega$  resistance in each phase. The PM-BLDC motor is driven by the same servo motor as in the feedback module test, where the speed is 500 rpm with the direction of CCW. The output ratio is set as 1 and 0.7, as measured in Fig. 21 (a) and (b), respectively. The proposed system can change the WPT frequency by sampling the value of  $V_p$ , generating a three-phase current output ( $i_U$ ,  $i_V$ ,  $i_{W}$ ) with a phase delay of 120 degrees. Although the output is transmitted under different frequencies at different times, the amplitude is nearly unchanged because of the modulation. When the output ratio is reduced, the output characteristic is maintained, while only the output amplitude is reduced. Both the PFM and PWM duty ratios are tuned to reach the desired output automatically, and the PFM achieves ZPA operation in  $f_1$  and  $f_3$  in the two output levels, as depicted in the zoomed waveforms.

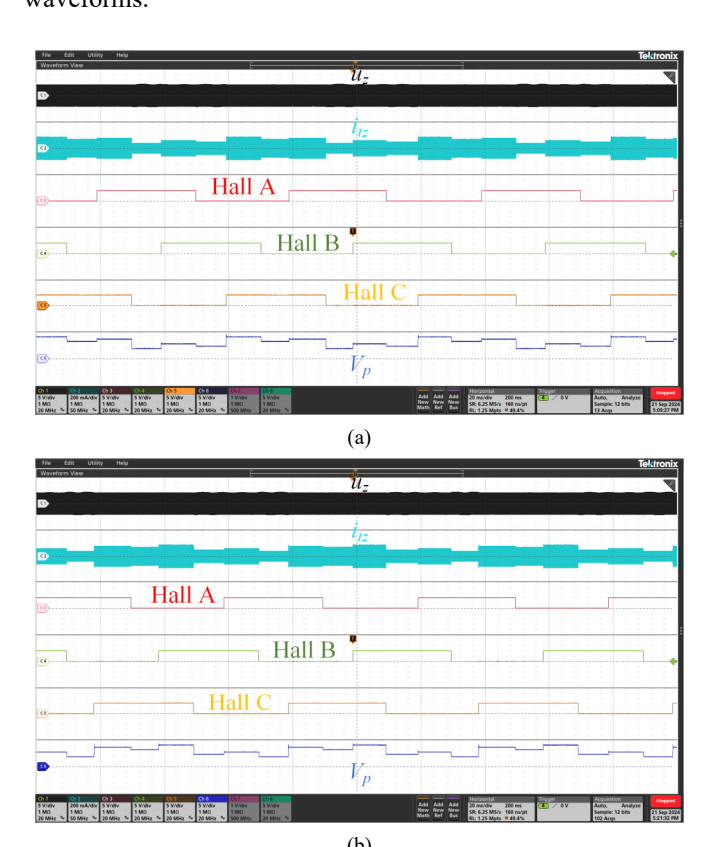


Fig. 20. Measured waveforms of feedback module when the motor is driven by a servo motor with a speed of 500 rpm. (a) Motor rotating in CCW direction. (b) Motor rotating in CW direction.

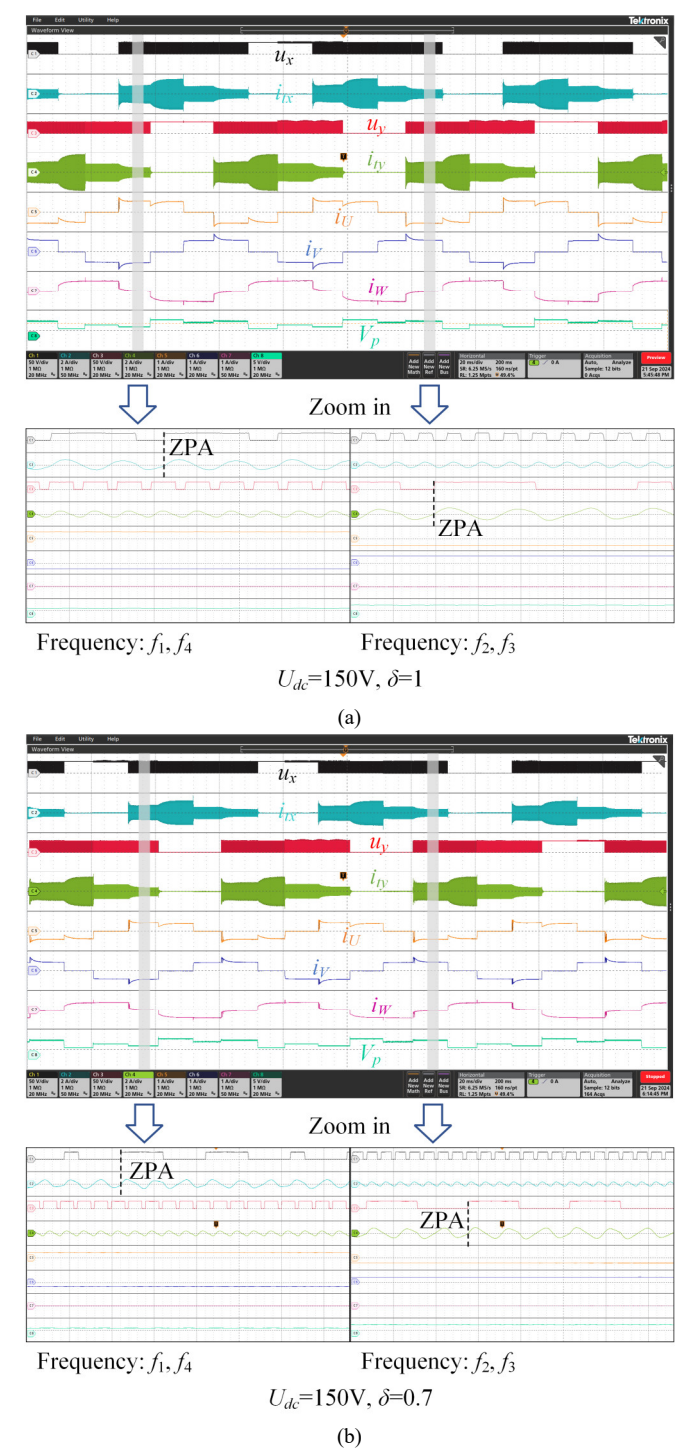


Fig. 21. Measured waveforms of proposed wireless PM-BLDC motor system using a three-phase Y-connected  $10-\Omega$  resistive load with an input voltage of 150 V. (a) Measured waveform when the output ratio is 1. (b) Measured waveforms when the output ratio is 0.7.

Fig. 22 shows the generation of switch control signals of the self-drive TPFS inverter at the secondary side.  $u_{Cax}$ ,  $u_{Cbx}$ ,  $u_{Cay}$ , and  $u_{Cby}$  denote the voltage over  $C_{ax}$ ,  $C_{bx}$ ,  $C_{ay}$ , and  $C_{by}$ .  $u_{GSAX}$ ,  $u_{GSBX}$ ,  $u_{BSAY}$ , and  $u_{GSBY}$  represent the gate-source voltage of the self-drive switches. The decoupled current paths formed by the compensation circuit provide independent control signals to the self-drive TPFS inverter. Only the targeted switch is turned on, while the untargeted switches are turned off.

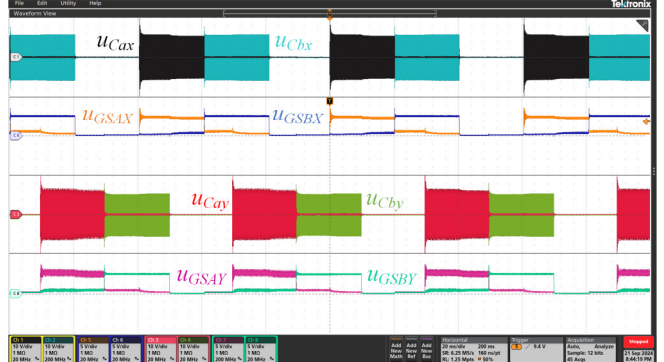


Fig. 22. Measured waveforms of switch control signals and voltages over signal generation capacitors.

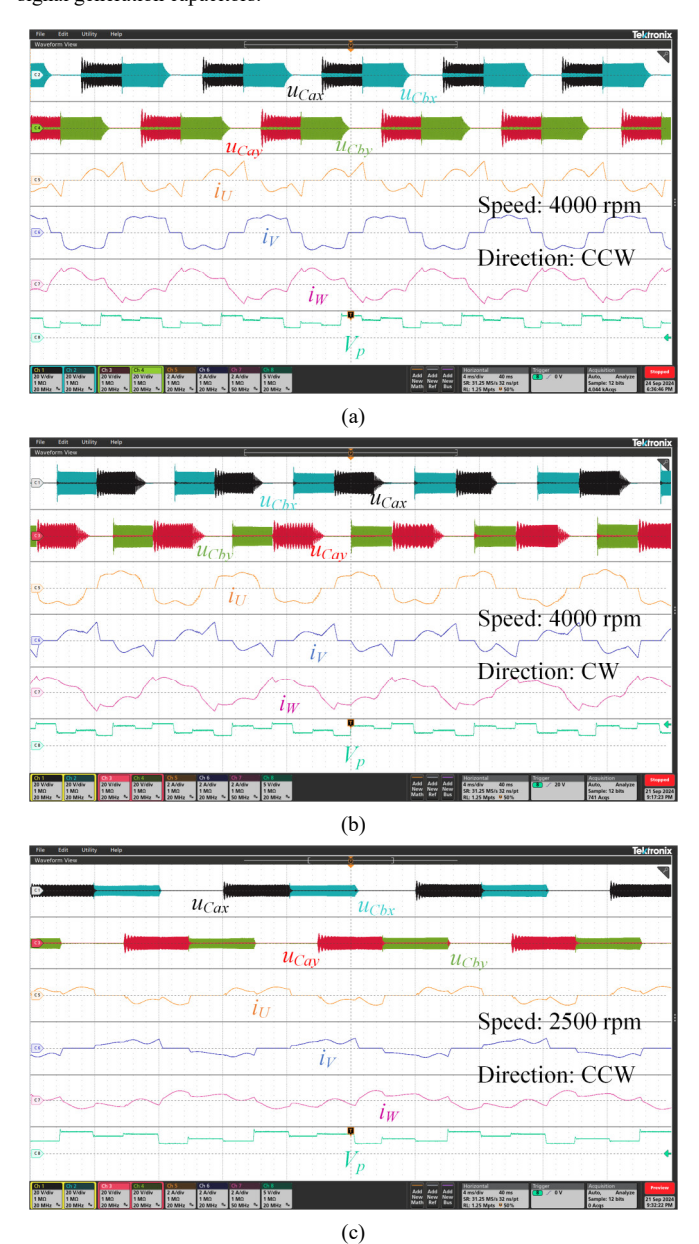


Fig. 23. Measured waveforms of proposed wireless PM-BLDC motor operating under different speeds and directions. (a) Rotating 4000 rpm CCW. (b) Rotating 4000 rpm CW. (c) Rotating 2500 rpm CCW.

Third, a three-phase PM-BLDC motor is loaded into the proposed system. The motor speed is first set to its rated value

of 4000 rpm, with a constant load torque of 20 N·cm. The DC input at the primary side is 250 V. Fig. 23 (a) and (b) shows the waveforms of the switch control signals, motor currents, and feedback signals when rotating in CCW and CW directions. Compared with the resistive load test waveforms in Fig. 21, the motor currents are no longer square waves, which is probably caused by the back EMF. Also, due to the usage of the TPFS inverter, only phases U and V are actively controlled, the unbalanced motor current induced by the back EMF distorts the current of phase W. Then, to verify the feasibility with a variable speed, the speed is then reduced to 2500 rpm with the same load, as shown in Fig. 23 (c). Wherein, the amplitude of currents is reduced to reach the target speed. Therefore, the proposed system can commutate autonomously according to contactless feedback in different speeds and directions and can reach a stable target speed via output modulation.

Finally, to verify the dynamic performance of the proposed PM-BLDC motor, the speed regulation characteristic is evaluated. The rotor positions recorded by an incremental are calculated by a DSP (TMS320F28379D), sampled at 200 Hz. Fig. 24 (a) shows the speed curve when alternating between 2500 rpm to 4000 rpm. The results show that the motor speed can reach the predefined value with a fast response and keeps constant at steady-state operation. Fig. 24 (b) shows the motor speed under a variable load, the motor starts operating with a load of 40 N·cm, and then reduces to 10 N·cm with the same step of 10 N·cm. The motor speed can recover from the disturbance of load variation in a short time, which further proves the feasibility of the proposed system. The system efficiency is also tested, under a 4000-rpm speed and 20-N·cm load condition, the power module efficiency is 73.5 % from the primary-side DC input to the motor terminals and the overall power consumption of the feedback module is 2.02 W.

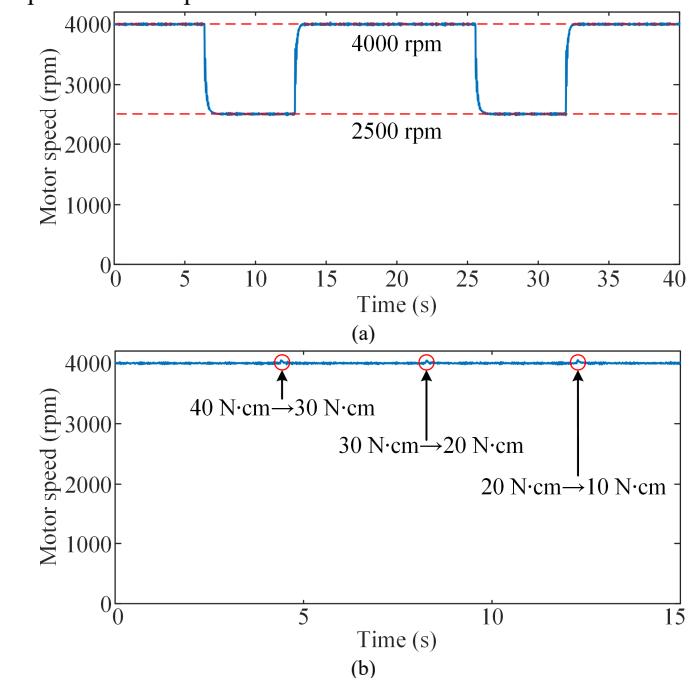


Fig. 24. Speed control characteristics of proposed wireless PM-BLDC motor under variable speed and variable load conditions. (a) Motor speed alternating between 2500 rpm and 4000 rpm. (b) Load variation with 4000 rpm speed.

TABLE II
COMPARISON OF EXISTING WIRELESS MOTORS AND PROPOSED WIRELESS PM-BLDC MOTOR

Ref.	Controller	Bidirectional motion	Motor type	Transfer distance	System efficiency	Speed control	Feedback
[12]	2 sides	Yes	PMSM	100 mm	88.8%	Yes	Yes
[15]	1 side	Yes	DC	100 mm	90%	No	No
[17]	1 side	No	SPIM	20 mm	77%	No	No
[18]	1 side	Yes	HSM	55 mm	76.97%	Yes	No
[20]	1 side	Yes	SRM	150 mm	72.8%	Yes	Yes
[26]	1 side	Yes	PM-BLDC	20 mm	80.2%	No	No
Proposed	1 side	Yes	PM-BLDC	55 mm	73.5%	Yes	Yes

# B. Discussion and Recommendation

The proposed wireless PM-BLDC motor is populated with precise speed control capability, showing unique advantages in practical applications. In the application of underground pipeline networks, the flow rate can be controlled easily to the expected value, keeping the pipe pressure below the threshold while maintaining a relatively high volume of transportation. A comprehensive comparison with the existing wireless motors is given in Table II to highlight the novelty of this design. It can be observed that most of the wireless motors with speed control capability need feedback from the sensors. The proposed design reaches the balance between real-time performance and the system size, satisfying the requirement of high-speed commutation with only one controller. The wireless HSM has open-loop speed control capability, however, the motor cannot detect the missed steps when the load exceeds the allowed range. Compared with wireless HSM, the proposed system has better reliability.

### VI. CONCLUSION

This article proposes and implements a brand-new wireless PM-BLDC motor. The proposed motor realizes a fully contactless approach for real-time position feedback. Through the design of the compensation circuit, the Hall effect sensor is powered wirelessly, and the modulated outputs can be sensed at the primary side. With a self-drive TPFS inverter connected to the motor, three-phase motor currents are generated with a reduced number of switches, and all the switches can be controlled by simply changing the transmitting frequency. Thus, the commutation and precise speed control are completed by a single controller at the primary side. The proposed system further combines  $\Sigma$ - $\Delta$  PFM and PWM for output regulation, which helps to achieve ZVS in part of the operation time and keeps a wide output range while suffering from fewer effects of harmonics. The motor speed can be controlled via contactless position feedback. Theoretical analysis, computer simulations, and experimental verifications have been conducted to verify the feasibility of the proposed PM-BLDC motor. The experimental results show that the proposed system can drive the motor to the speed of 4000 rpm and shows great dynamic performance in speed and load variations.

### REFERENCES

- Y. Wang, Z. Sun, Y. Guan, and D. Xu, "Overview of megahertz wireless power transfer," *Proc. IEEE*, vol. 111, no. 5, pp. 528-554, May 2023.
- [2] D. Patil, M. K. McDonough, J. M. Miller, B. Fahimi, and P. T. Balsara, "Wireless power transfer for vehicular applications: Overview and challenges," *IEEE Trans. Transp. Electrif.*, vol. 4, no. 1, pp. 3-37, Mar. 2018.

- [3] G. A. Covic and J. T. Boys, "Inductive power transfer," *Proc. IEEE*, vol. 101, no. 6, pp. 1276-1289, Jun. 2013.
- [4] S. Li and C.C. Mi, "Wireless power transfer for electric vehicle applications," *IEEE J. Emerg. Sel. Topics Power Electron.*, vol. 3, no. 1, pp. 4-17, Mar. 2015.
- [5] J. Feng, Q. Li, F.C. Lee, and M. Fu, "Transmitter coils design for free-positioning omnidirectional wireless power transfer system," *IEEE Trans. Ind. Inform.*, vol. 15, no. 8, pp. 4656-4664, Aug. 2019.
- [6] L. Wu, B. Zhang, and J. Zhou, "Efficiency improvement of the parity-time-symmetric wireless power transfer system for electric vehicle charging," *IEEE Trans. Power Electron.*, vol. 35, no. 11, pp. 12497-12508, Nov. 2020.
- [7] Z. Deng, H. Hu, Y. Su, F. Chen, J. Xiao, C. Tang, and T. Lin, "Design of a 60-kW EV dynamic wireless power transfer system with dual transmitters and dual receivers," *IEEE J. Emerg. Sel. Topics Power Electron.*, vol. 12, no. 1, pp. 316-327, Feb. 2024.
- [8] K. Chen and Z. Zhang, "In-flight wireless charging: A promising application-oriented charging technique for drones," *IEEE Ind. Electron. Mag.*, vol. 18, no. 1, pp. 6-16, Mar. 2024.
- [9] H. Pang, F. Xu, W. Liu, C.K. Tse, and K.T. Chau, "Impedance buffer-based reactance cancellation method for CLC-S compensated wireless power transfer," *IEEE Trans. Ind. Electron.*, vol. 71, no. 7, pp. 6894-6906, Jul. 2024.
- [10] J. Cai, B. Li, W. Hua, A. D. Cheok, Y. Yan, and X. Zhang, "Magnetic coupled wireless motor driving systems-An overview," *IEEE Trans. Power Electron.*, vol. 39, no. 6, pp. 7375-7391, Jun. 2024.
- [11] W. Liu, K.T. Chau, X. Tian, H. Wang, and Z. Hua, "Smart wireless power transfer-Opportunities and challenges," *Renewable Sustain*. *Energy Rev.*, vol. 180, Jul. 2023, Art. no. 113298.
- [12] M. Sato, G. Yamamoto, D. Gunji, T. Imura, and H. Fujimoto, "Development of wireless in-wheel motor using magnetic resonance coupling," *IEEE Trans. Power Electron.*, vol. 31, no. 7, pp. 5270-5278, Jul. 2016.
- [13] C. Li, Z. Wang, and Y. Xu, "A wireless-power-transfer-based three-phase PMSM drive system with matrix converter," *IEEE Trans. Ind. Electron.*, vol. 70, no. 3, pp. 2307-2317, Mar. 2023.
- [14] Y. Chen, C. Gan, H. Shi, K. Ni, Z. Yang, and R. Qu, "Auxiliary circuit free maximum power efficiency tracking scheme for wireless motor system with source-load coupling," *IEEE Trans. Ind. Electron.*, vol. 70, no. 4, pp. 3414-3425, Apr. 2023.
- [15] H. Liu, H. Zhou, Q. Deng, W. Hu, X. Gao, and L. Fang, "A wireless DC motor drive using LCCC-CCL compensated network with bidirectional motion capability," *IEEE Trans. Circuits Syst. I: Regul. Pap.*, vol. 69, no. 11, pp. 4714-4725, Nov. 2022.
- [16] L. Fang, H. Zhou, W. Hu, J. Chen, A. Zhu, X. Gao, and Q. Deng, "Design of wireless individual-drive system for variable-reluctance stepping motor," *IEEE Trans. Circuits Syst. II Express Briefs*, vol. 69, no. 4, pp. 2141-2145, Apr. 2022.
- [17] H. Wang, K.T. Chau, C.H.T. Lee, and C. Jiang, "Wireless shaded-pole induction motor with half-bridge inverter and dual-frequency resonant network," *IEEE Trans. Power Electron.*, vol. 36, no. 12, pp. 13536-13545, Dec. 2021.
- [18] S. Li, K.T. Chau, W. Liu, C. Liu, and C.K. Lee, "Design and control of wireless hybrid stepper motor system," *IEEE Trans. Power Electron.*, vol. 39, no. 8, pp. 10518-10531, Aug. 2024.
- [19] W. Liu, K.T. Chau, C.H.T. Lee, L. Cao, and W. Han, "Wireless power and drive transfer for piping network," *IEEE Trans. Ind. Electron.*, vol. 69, no. 3, pp. 2345-2356, Mar. 2022.
- [20] C. Jiang, K.T. Chau, C. Liu and W. Han, "Design and analysis of wireless switched reluctance motor drives," *IEEE Trans. Ind. Electron.*, vol. 66, no. 1, pp. 245-254, Jan. 2019.

- [21] H. Wang, K.T. Chau, C.H.T. Lee, and X. Tian, "Design and analysis of wireless resolver for wireless switched reluctance motors," *IEEE Trans. Ind. Electron.*, vol. 70, no. 3, pp. 2221-2230, Mar. 2023.
- [22] Y. Liu, W. Wang, S. Liu, and C. Liu, "A compact wireless permanent magnet synchronous motor system with precise speed and position control," *IEEE Trans. Ind. Electron.*, vol. 71, no. 10, pp. 11852-11863, Oct. 2024.
- [23] D. Mohanraj, R. Aruldavid, R. Verma, K. Sathiyasekar, A. B. Barnawi, B. Chokkalingam, L. Minet-popa, "A review of BLDC motor: State of art, advanced control techniques, and applications," *IEEE Access*, vol. 10, pp. 54833-54869, 2022.
- [24] C. Xia, Permanent magnet brushless DC motor drives and controls. Singapore: John Wiley & Sons, 2012.
- [25] J. Tang, Q. Zhang, C. Cui, T. Na, and T. Hu, "An improved hybrid frequency pacing modulation for wireless power transfer systems," *IEEE Trans. Power Electron.*, vol. 36, no. 11, pp. 12365-12374, Nov. 2021.
- [26] H. Wang, K.T. Chau, W. Liu, and S. M. Goetz, "Design and control of wireless permanent-magnet brushless DC motors," *IEEE Trans. Energy Convers.*, vol. 38, no. 4, pp. 2969-2979, Dec. 2023.
- [27] W. Han, K.T. Chau, Z. Hua, and H. Pang, "Compact wireless motor drive using orthogonal bipolar coils for coordinated operation of robotic arms," *IEEE Trans. Magn.*, vol. 58, no. 2, Feb. 2022, Art. no. 8200608.
- [28] J. Lu, G. Zhu, D. Lin, Y. Zhang, J. Jiang, and C. C. Mi, "Unified load-independent ZPA analysis and design in CC and CV modes of higher order resonant circuits for WPT systems," *IEEE Trans. Transp. Electrif.*, vol. 5, no. 4, pp. 977-987, Dec. 2019.
- [29] K. Song, Z. Li, J. Jiang, and C. Zhu, "Constant current/voltage charging operation for series-series and series-parallel compensated wireless power transfer systems employing primary-side controller," *IEEE Trans. Power Electron.*, vol. 33, no. 9, pp. 8065-8080, Sept. 2018.
- [30] X. Liu, R. Chen, F. Li, D. Zhou, and J. Zou, "A WPT system with DC-link series/parallel AC-link parallel rectifiers for AUVs with multiple charging voltages and currents," *IEEE Trans. Power Electron.*, vol. 39, no. 8, pp. 10605-10617, Aug. 2024.
- [31] X. Wang, M. Leng, X. Zhang, H. Ma, B. Guo, J. Xu, and C.K. Lee, "Synthesis and analysis of primary high-order compensation topologies for wireless charging system applying sub-harmonic control," *IEEE Trans. Power Electron.*, vol. 38, no. 7, pp. 9173-9182, Jul. 2023.
- [32] H. Zhang, W. Liu, Z. Li, and C.K. Lee, "Pulse frequency modulation of 3D wireless power transfer for capsule endoscopy," *IEEE Trans. Ind. Electron.*, vol. 72, no. 1, pp. 308-317, Jan. 2025.



Songtao Li (Student member, IEEE) received the B.Eng and M.Eng degrees in instrument science and technology from Southeast University, Nanjing, China in 2018 and 2021, respectively. He is currently working toward the Ph.D. degree in electrical and electronic engineering in the University of Hong Kong, Hong Kong, China.

His current research interests include power electronics, wireless power transfer, and electric vehicle technologies.



K. T. Chau (Fellow, IEEE) received the B.Sc. (Eng.), M.Phil., and Ph.D. degrees in electrical and electronic engineering from The University of Hong Kong, Hong Kong, in 1988, 1991, and 1993, respectively. Currently, he serves as Chair Professor of Electrical Energy Engineering at the Research Centre for Electric Vehicles and Department of Electrical and Electronic Engineering, The Hong Kong Polytechnic University. His research interests include electric and hybrid vehicles, power

electronics and drives, and renewable energies. He is the author of nine books and more than 350 journal papers.

Prof. Chau is a Fellow of the Institution of Engineering and Technology (IET), U.K., and of the Hong Kong Institution of Engineers. He is also a Coeditor of the Journal of Asian Electric Vehicles. He is a Chartered Engineer. He was the recipient of the Changjiang Chair Professorship from the Ministry of Education, China, and the Environmental Excellence in Transportation

Award for Education, Training, and Public Awareness from the Society of Automotive Engineers International.



Wei Liu (Senior Member, IEEE) received the B.Eng. and M.Eng. degrees in electrical engineering from China University of Petroleum, Qingdao, China, and a Ph.D. degree in electrical and electronic engineering from The University of Hong Kong (HKU), Hong Kong, China, in 2014, 2017, and 2021, respectively.

He is currently an Assistant Professor at the Research Centre for Electric Vehicles and Department of Electrical and Electronic Engineering,

The Hong Kong Polytechnic University (PolyU). Dr. Liu served as a Postdoctoral Fellow and a Research Assistant Professor from 2021 to 2023, and he is now an Honorary Assistant Professor at the Department of Electrical and Electronic Engineering, HKU. He also worked as a Visiting Researcher with Nanyang Technological University, Singapore (NTU), in 2019. His research interests include wireless power transfer, power electronics, biomedical power electronics, and electric vehicle technologies.

Dr. Liu was the recipient of the Power Engineering Prize from HKU, the Excellent Paper Award, and the Best Presentation Award from international conferences in the area of Electric Vehicles and Transportation Electrification. He is also a Guest Associate Editor of *IEEE Journal of Emerging and Selected Topics in Power Electronics (JESTPE)*, Guest Editor of international journals, and Session Chair of international conferences.



Jian Guo (Member, IEEE) was born in Hubei, China, in 1995. He received a B.S. degree in electronic information engineering from China University of Mining and Technology, Xuzhou, China, in 2017, and a Ph.D. degree in electrical engineering from Hunan University, Changsha, China, in 2022. Currently, he is a Postdoctoral Fellow in electrical and electronic engineering at the Department of Electrical and Electronic Engineering, at the University of Hong Kong. His research interests include power electronic converters, wireless power transfer, and renewable energies.



Chunhua Liu (Senior Member, IEEE) received the B.Eng. and M.Eng. degrees in Automatic Control from Beijing Institute of Technology, China, and Ph.D. degree in Electrical and Electronic Engineering from The University of Hong Kong, Hong Kong SAR, in 2002, 2005 and 2009, respectively.

Since 2015, he has been with City University of Hong Kong, Hong Kong SAR, where he is currently a Professor in Electrical and Electronic Engineering

with the School of Energy and Environment. His research interests include electric machines and drives, electric vehicles and aircrafts, electric robotics and ships, renewables and microgrids, power electronics and wireless power transfer. In these areas, he has published over 300 refereed papers. In addition, he is an RGC Research Fellow, Distinguished Lecturer of IEEE Vehicular Technology Society (VTS), and World's Top 2% Scientists according to metrics compiled by Stanford University.

Prof. Liu is now an Associate Editor of IEEE Transactions on Industrial Electronics, Editor of IEEE Transactions on Vehicular Technology, Editor of IEEE Transactions on Energy Conversion, and Editor of IEEE Power Engineering Letters. Also, he is an Editor of Energies, Subject Editor of IET – Renewable Power Generation, Associate Editor of Open Journal of the Industrial Electronics Society, Associate Editor of IEEE Access; Associate Editor of IEEE Chinese Journal of Electrical Engineering, Associate Editor of CES Transactions on Electrical Machines and Systems, Associate Editor of Elsevier Green Energy and Intelligent Transportation, and Editor of IEEE Transactions on Magnetics – Conference, respectively. In addition, he is Chair & Founder of both Hong Kong Chapter, IEEE Vehicular Technology Society, and Hong Kong & Guangzhou Joint Chapter, IEEE Industrial Electronics Society, respectively.



Yunhe Hou (Senior Member, IEEE) received the B.E. and Ph.D. degrees in electrical engineering from the Huazhong University of Science and Technology, Wuhan, China, in 1999 and 2005, respectively. He was a Postdoctoral Research Fellow with Tsinghua University, Beijing, China, from 2005 to 2007, and a Postdoctoral Researcher with Iowa State University, Ames, IA, USA, and the University College Dublin, Dublin, Ireland, from 2008 to 2009. He was also a Visiting Scientist with the Laboratory for Information and Decision Systems,

Massachusetts Institute of Technology, Cambridge, MA, USA, in 2010. He has been a Guest Professor at the Huazhong University of Science and Technology, China, since 2017, and an Academic Adviser at China Electric Power Research Institute from 2019. He joined the Faculty of the University of Hong Kong, Hong Kong, in 2009, where he is an Associate Professor in the Department of Electrical and Electronic Engineering. He was an Associate Editor of IEEE TRANSACTIONS ON SMART GRID from 2016 to 2021. He is currently an Associate Editor of IEEE TRANSACTIONS POWER SYSTEMS and Journal of Modern Power Systems and Clean Energy.